Elaborately tailored $NiCo_2O_4$ for highly efficient overall water splitting and urea electrolysis

Yamei Wang [a], Lanli Chen [b, c], Huaming Zhang [a,*], Muhammad Humayun [b], Junhong Duan [a], Xuefei Xu [d], Yanjun Fu [a], Mohamed Bououdina [b], Chundong Wang [d,b,*]

[a] Jiangxi Province Key Laboratory of Optoelectronic Information Science and Technology, Nanchang Hangkong University, Nanchang 330063, Jiangxi, China

[b] Energy, Water and Environment Lab, College of Humanities and Sciences, Prince Sultan University, Riyadh 11586, Saudi Arabia

[c] School of Mathematics and Physics, Hubei Polytechnic University, Huangshi 435003, PR China

[d] School of Integrated Circuits, Wuhan National Laboratory for Optoelectronics, Huazhong University of Science and Technology, Wuhan 430074, P.R. China

Email: 70451@nchu.edu.cn (H.M. Zhang); apcdwang@hust.edu.cn (C.D. Wang)

[*] Corresponding authors 70451@nchu.edu.cn (H.M. Zhang); apcdwang@hust.edu.cn (C.D. Wang)

1. Experimental materials and calculation methods

1.1 Chemical Materials

Commercial products of Pt/C (20 wt.% Pt on Vulcan XC-72R) were received from Sigma Aldrich and RuO_2 catalysts were obtained from Aladdin Co., Ltd. Shanghai China. Nickel foam (NF) with a density of 0.29 g cm^{-3} and 120 pores per inch (SEM images with thickness of 1 mm) was obtained from the Kunshan Zhenyuhongxin Materials Co., Ltd. China. Ruthenium (III) chloride hydrate ($RuCl_3 \cdot xH_2O$, purity 99.9%, Ru content 35-42%), ammonium fluoride (NH_4F), urea ($CO(NH)_2$), and cobalt-(II) nitrate hexahydrate ($Co(NO_3)_2 \cdot 6H_2O$) were ordered from Aladdin Company. The Beijing Chemicals Reagent Factory, ethanol (CH_3CH_2OH), and hydrochloric acid (HCl, ca. 36-38%). Millipore system was utilized to produce the deionized (DI) water for the tests. All chemicals utilized were of an analytical standard and used as received.

1.2 Characterization

Several analytical methods were used to characterize the as-obtained sample's compositions and microstructures. X-ray diffraction (XRD) technique was used to characterize the crystal phases of the catalysts in the range of 10-80° (10° min^{-1} scan rate). The morphology was studied using both a field-emission scanning electron microscope (Zeiss-G-300, FESEM) and a transmission electron microscope (TEM; FEI-Tecnai-TM G2F30). The sample's microscopic morphology and microstructure were explored via the high-resolution TEM (HR-TEM) and high angle-annular dark-field scanning TEM (HAADF-STEM). All electrocatalyst's chemical compositions and states were verified via the X-ray photoelectron spectroscopy ((XPS) using the Al Kα X-ray source (providing photons with 1486.6 eV). The pore distribution and N_2 adsorption/desorption isotherms were measured with an ASAP2460 equipment. The amounts of

Ru, Co, Ni and O in catalysts were determined by Inductively Coupled Plasma Optical Emission Spectrometry (ICP-OES, Agilent ICPOES 720ES).

1.3 Electrochemical measurement

The CHI-760E electrochemical workstation (Chenhua Instruments, Shanghai, China) was used to conduct the tests on a typical three-electrode setup for the electrochemical analysis. Working electrode was the as-prepared catalyst (1 × 1 cm^2), a graphite rod was employed as the counter electrode, and Hg/HgO saturated KOH as the reference electrode. After cycling 30 times to produce a steady cyclic voltammetry (CV) curve, the polarization curves of the catalysts were analyzed using linear-sweep voltammetry (LSV) at a scan rate of 1 mV s^{-1}. For all polarization curves presented in the paper, the iR values were 95% manually corrected with the series resistance (R_s) on the basis of the equation: $E_{RHE} = E_{Hg/HgO} + 0.059pH + E^{\circ}_{Hg/HgO} - iR_s$, with $E^{\circ}_{Hg/HgO}$=0.098V versus SHE, where the compensated ohmic R_s values were obtained from the fittings of electrochemical impedance spectra. The Tafel's equation η= blog j + a, where b is the slope and j is the current density, can be used to learn more about the reactions' mechanism. In order to perform electrochemical-impedance spectroscopy (EIS) studies, the potential scanning was halted at varying potentials, and the resulting impedance-spectra were recorded throughout a frequency range of 1 MHz to 0.01 Hz. In addition, the non-faradaic potential regions' double-layered capacitance (C_{dl}) was used to predict the electrochemical active-surface-areas (ECSA), and the value of ECSA is given by the equation ECSA=C_{dl}/C_s with $C_s \approx 0.04$ mF cm^{-2}. Herein, by plotting the capacitive currents (Δ j =janodic − jcathodic) versus the corresponding scan rates, the C_{dl} can be predicted as a half of the slope. The stability of these as-prepared catalysts was tested by chronopotentiometric method.

Calculation of TOF:

The Turnover frequency (TOF) is a relevant and useful kinetic parameter to explore the intrinsic activity of catalysts. Based on following assumption: i) All metal ions in the catalysts are active and contributed to the catalytic reaction (the lowest TOF values), ii) Active sites are uniformly distributed in the catalyst, TOFs for OER and HER were calculated with the following equations:

$$TOF = \frac{j(\eta) \times A}{n \times F \times m}$$

where "j(η)" is the measured current density ($A \cdot cm^{-2}$) at an overpotential of η, "A" is the surface area of the integrated electrode (1 cm^2), "n" is the number of transferred electrons to generate a molecule of product (n = 4 for OER, n = 2 for HER), "F" stands for the Faraday constant (96485 C mol^{-1}), "m" is the number of participating atoms or active sites in the as-prepared samples, which was determined based on ICP-OES.

1.4 Theoretical calculations

The Vienna ab *initio* simulation software (VASP) was used to run the simulations, which were based on a plane wave density functional[1,2]. The generalized gradient approximation (GGA) of Perdew-Burke-Ernzerhof (PBE) was used to deal with the exchange-correlation section of the density functional, and the corresponding potentials were of the projector augmented wave (PAW) sort[3,4]. The $NiCo_2O_4$ (110) surface was modeled using a 4x4x1 Monkhorst-Pack k-point mesh with Gaussian smearing of 0.15 eV and a plane-wave energy cutoff of 450 eV. The energies have converged to a value of 10-5 eV/unit cell. Lower than 0.02 eV/Å convergence was achieved for the Hellman-Feynman forces. To prevent layer-to-layer interactions, we settled on a 15Å thick z-axis vacuum. The base is held steady while the other layers are allowed to relax up.

The adsorption energy (E_{ads}) was calculated as $E_{ads} = E_{adsorbed} - E_{pristine} - E_{adsorbate}$, where $E_{adsorbed}$, $E_{pristine}$, and $E_{adsorbate}$ are the total energies of the adsorbed system, the pristine system, and the adsorbate, respectively.

The following formula is used to calculate the free energies: $\Delta G = \Delta E + \Delta E_{ZPE} - T\Delta S$, where ΔE, ΔE_{ZPE}, and ΔS respectively denote the binding energy, zero-point energy change, and the entropy variation of the adsorption of adsorbates.

Calculation method of HER activity: $H^+ + e^- + {}^* \rightarrow \mathrm{H}^*$, where * represents the adsorption site. The computational hydrogen electrode model developed by Norskov was used to calculate the ΔG of the electrochemical elementary step. $\Delta G_{\mathrm{H}^*} = \Delta E_{\mathrm{H}^*} + \Delta E_{ZPE} - T\Delta S_{\mathrm{H}}$, where ΔE_{H^*} represent the energy difference of hydrogen adsorption by DFT calculation. ΔE_{ZPE} represents the difference between the zero-point energy of adsorbed hydrogen and gas phase hydrogen. $T\Delta S$ is the change of entropy at 298 K.

References

1 G. Kresse, J. Hafner, Ab initio molecular dynamics for liquid metals, *Phys. Rev. B* 47 (1993) 558(R).

2 G. Kresse, J. Furthmuller, Efficiency iterative schemes for ab initio total-energy calculations using a plane-wave basis set, *Phys. Rev. B* 54 (1996) 11169-11186.

3 J. P. Perdew, K. Burke, M. Ernzerhof, Generalized gradient approximation made simple, *Phys. Rev. Lett.* 77 (1996) 3865-3868.

4 P. E. Blochl, Projector augmented-wave method, *Phys. Rev. B* 50 (1994) 17953-17979.

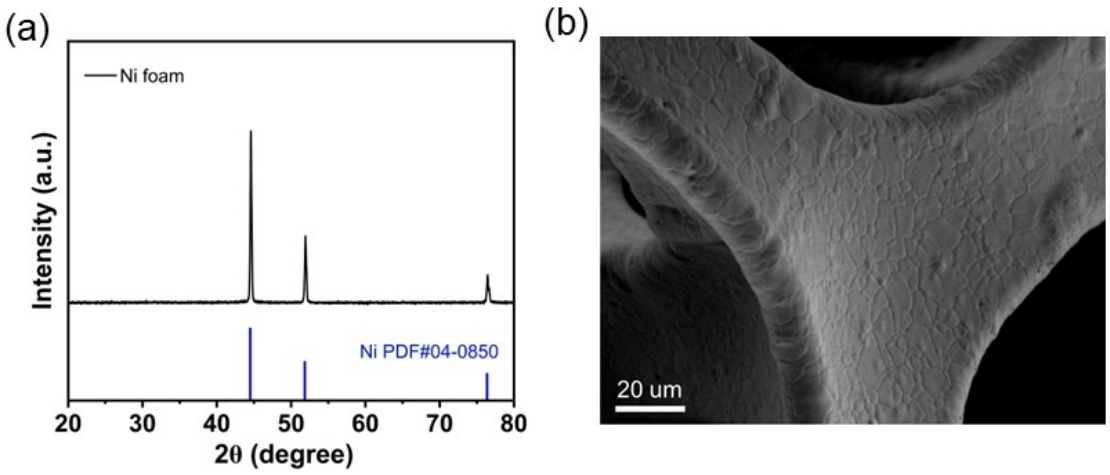

Figure S1. (a) XRD patterns and (b) SEM image of bare NF.

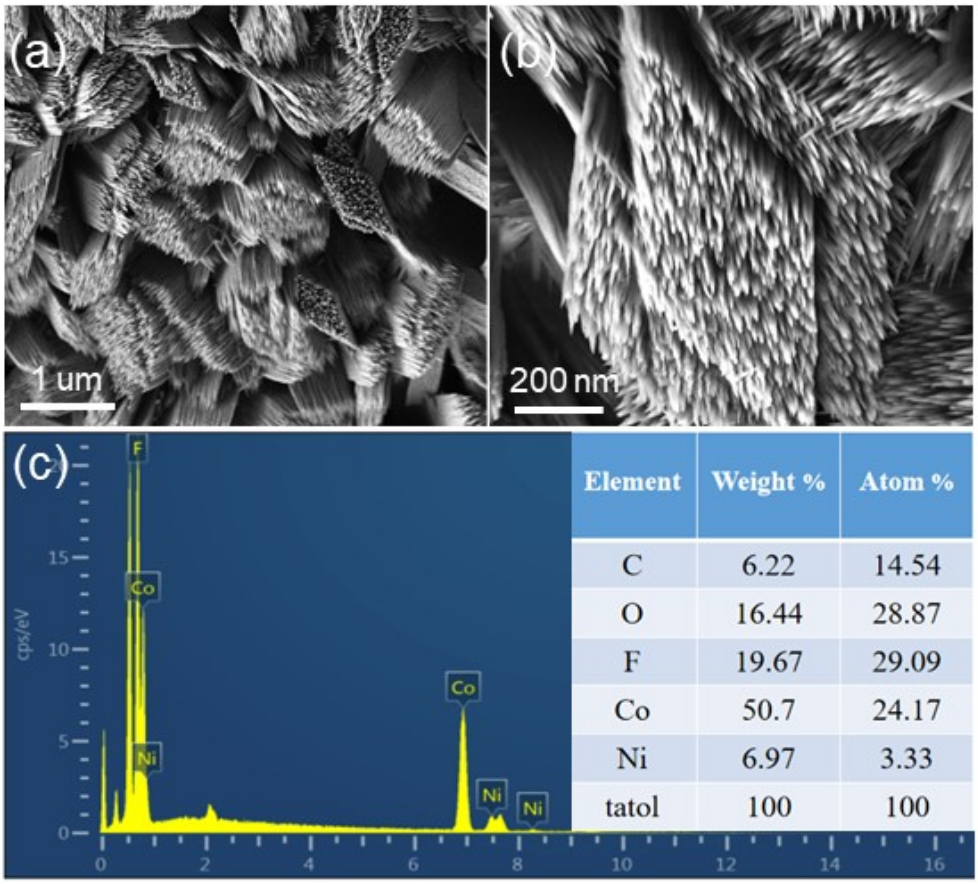

Element	Weight %	Atom %
C	6.22	14.54
O	16.44	28.87
F	19.67	29.09
Co	50.7	24.17
Ni	6.97	3.33
tatol	100	100

Figure S2. (a) low- resolution and (b) high- resolution SEM images of Co(OH)F. (b) EDS spectrum of Co(OH)F

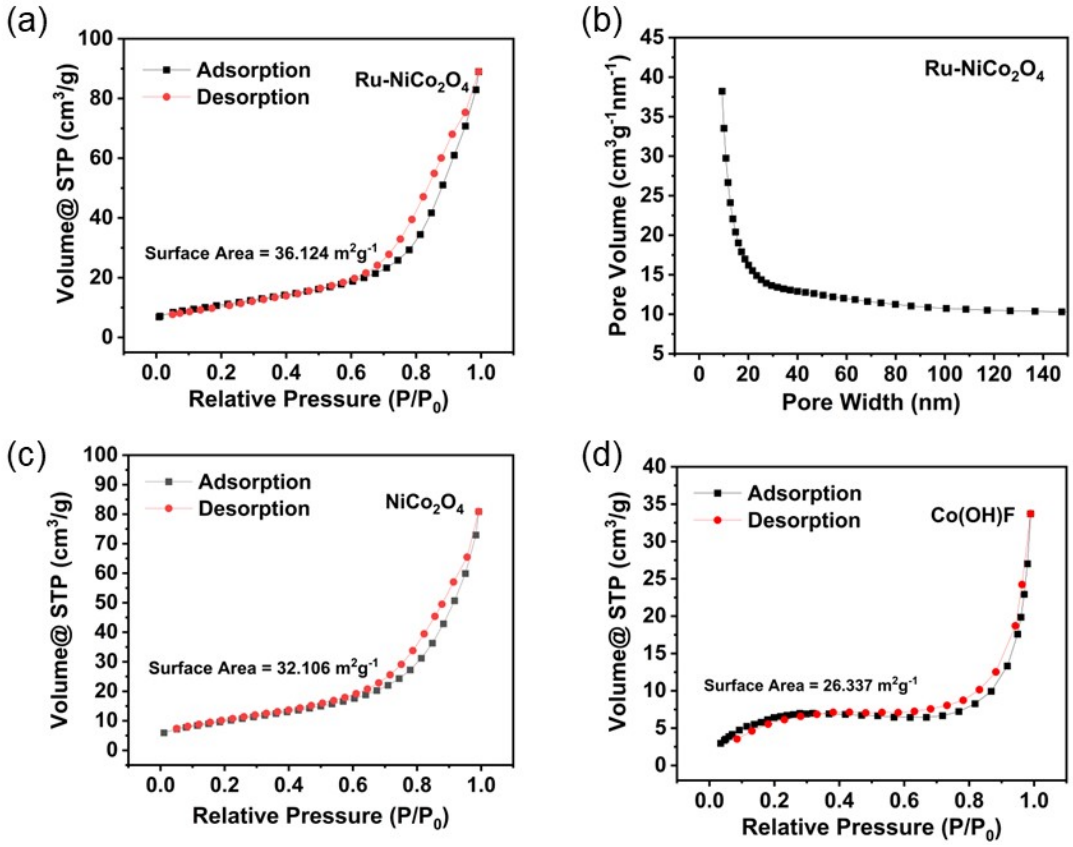

Figure S3. Nitrogen adsorption-desorption isotherms of (a) Ru-$NiCo_2O_4$ and (b) The image of corresponding pore size distribution, (c) $NiCo_2O_4$, (d) Co(OH)F.

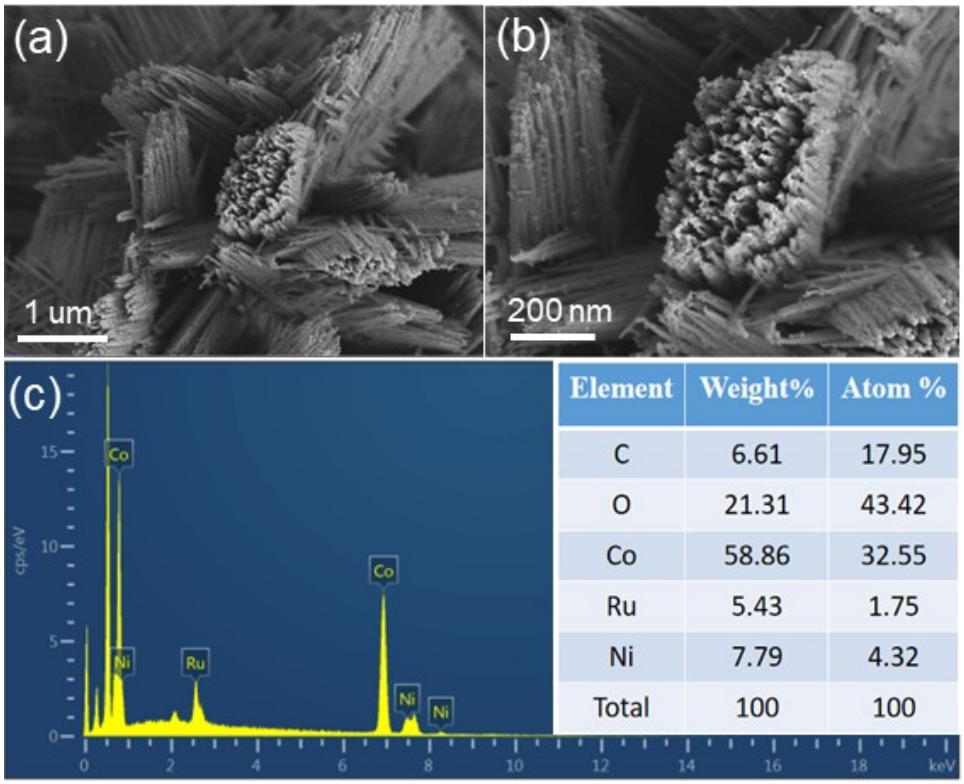

Element	Weight%	Atom %
C	6.61	17.95
O	21.31	43.42
Co	58.86	32.55
Ru	5.43	1.75
Ni	7.79	4.32
Total	100	100

Figure S4. (a) low-resolution, (b) high-resolution SEM images and (c) EDS spectrum of Ru-$NiCo_2O_4$.

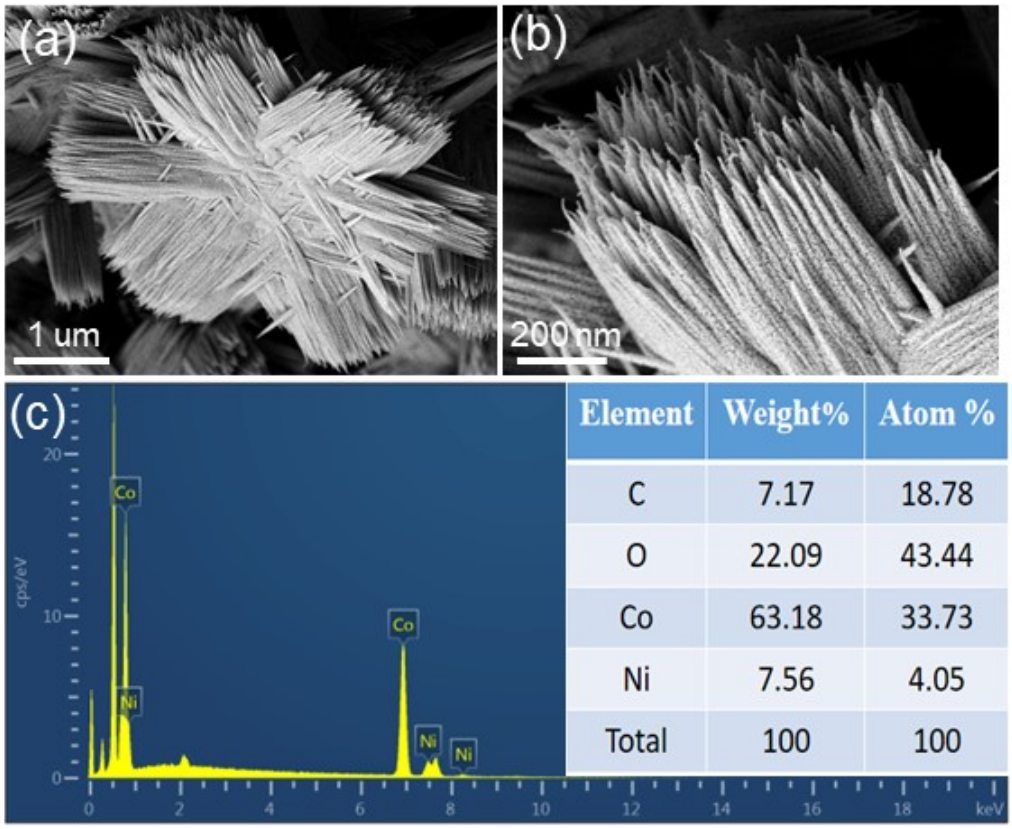

Element	Weight%	Atom %
C	7.17	18.78
O	22.09	43.44
Co	63.18	33.73
Ni	7.56	4.05
Total	100	100

Figure S5. (a) low- resolution and (b) high- resolution SEM images and (c) EDS spectrum of $NiCo_2O_4$.

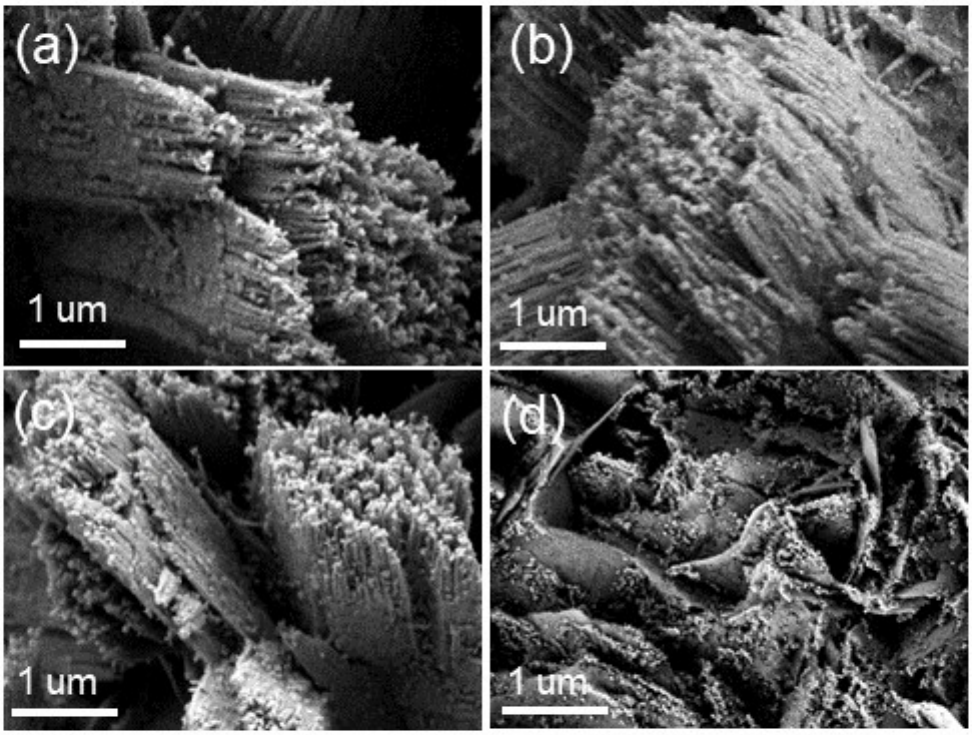

Figure S6. (a-d) SEM images of different Ru dosage at 0.01 M, 0.015 M, 0.025 M, and 0.03 M.

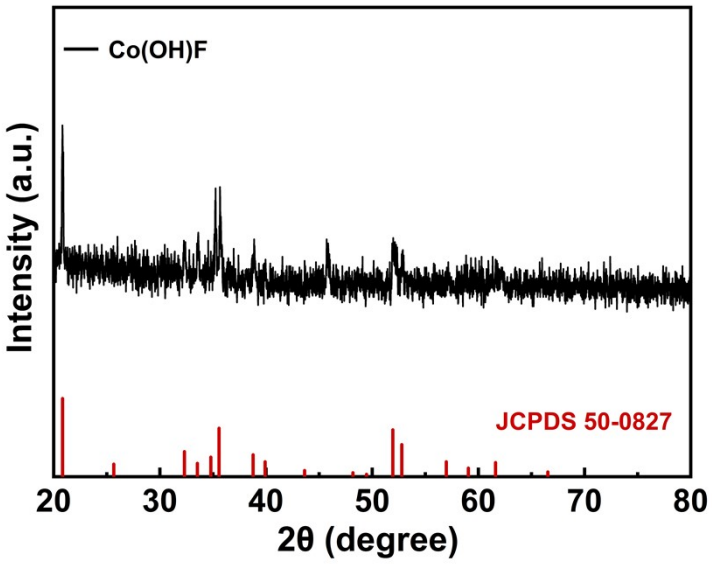

Figure S7. The XRD image of Co(OH)F.

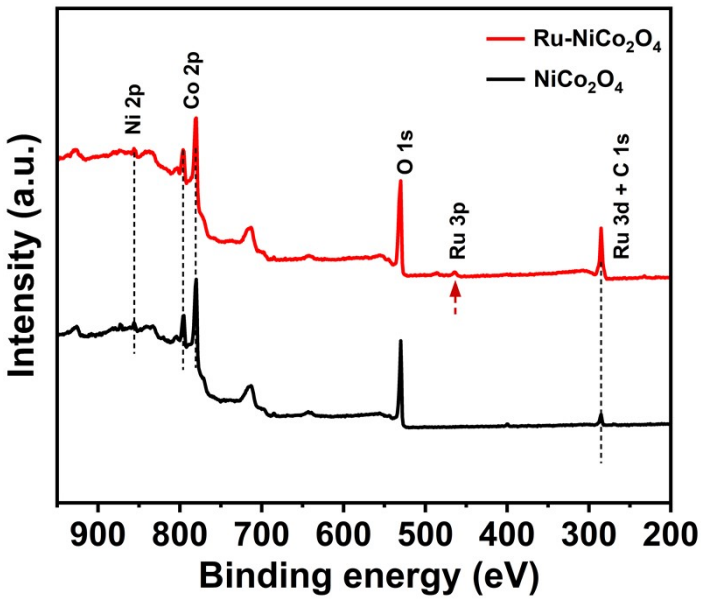

Figure S8. The XPS survey spectra of Ru-NiCo2O4 and NiCo2O4.

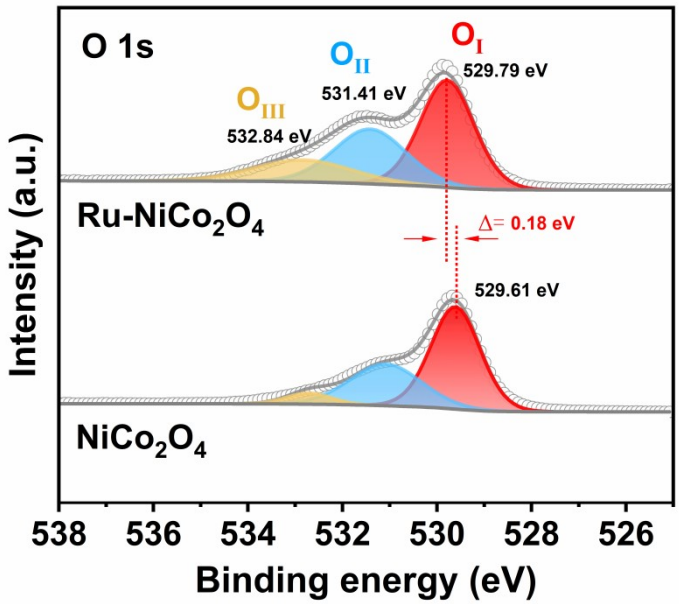

Figure S9. The XPS spectrum of O 1s in Ru-$NiCo_2O_4$ and $NiCo_2O_4$.

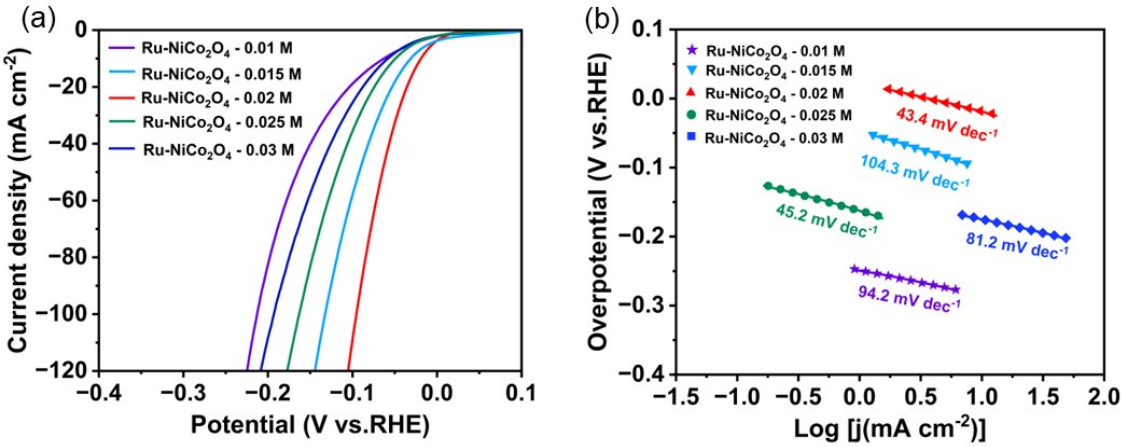

Figure S10. (a) the linear-sweep voltammetry (LSV) polarization-curves (b) the Tafel slope of Ru-$NiCo_2O_4$ with different concentration.

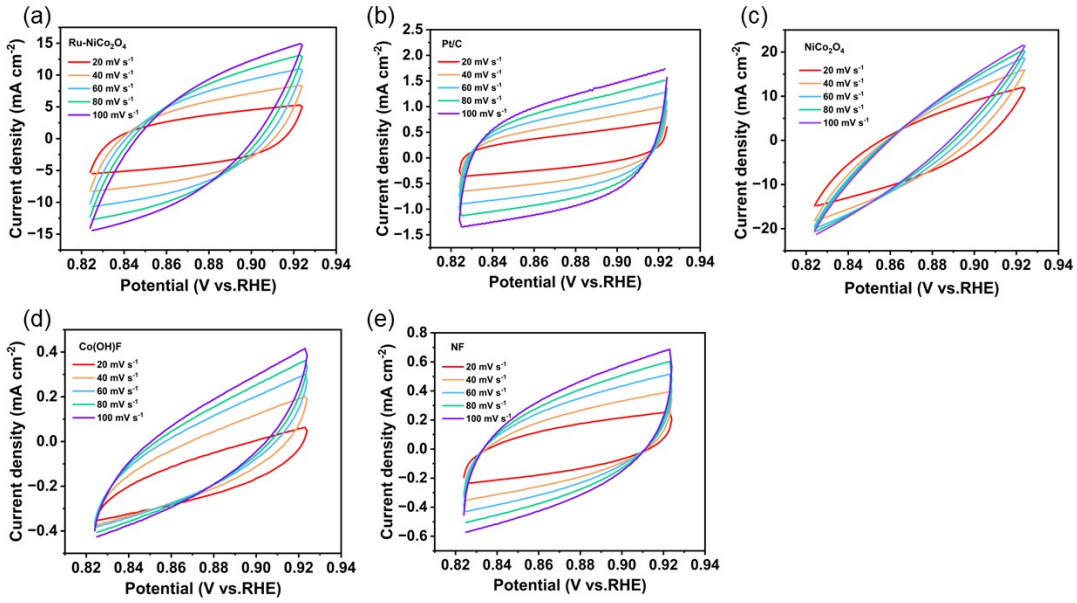

Figure S11. CV curves of the catalysts recorded in the region of 0.824-0.924 V for HER in 1 M KOH. (a) Ru-$NiCo_2O_4$, (b) Pt/C, (c) $NiCo_2O_4$, (d) Co(OH)F, (e) NF.

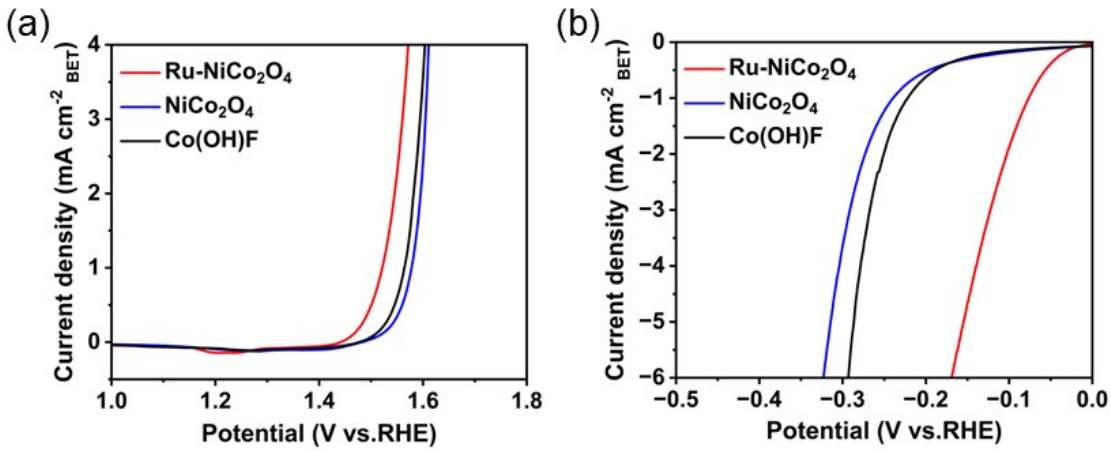

Figure S12. The normalized LSV curve for HER (a) and OER (b) of Ru-$NiCo_2O_4$, $NiCo_2O_4$ and Co(OH)F based on the BET surface area.

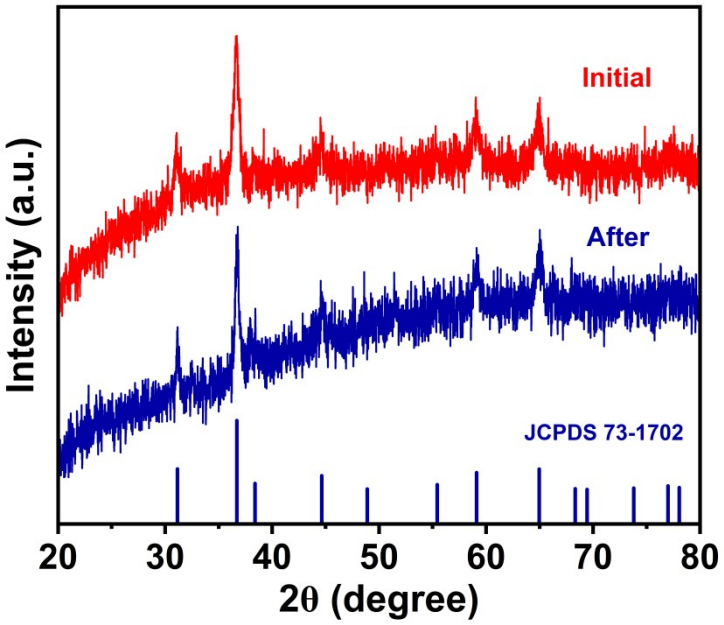

Figure S13. XRD of the Ru-$NiCo_2O_4$ catalyst after HER stability.

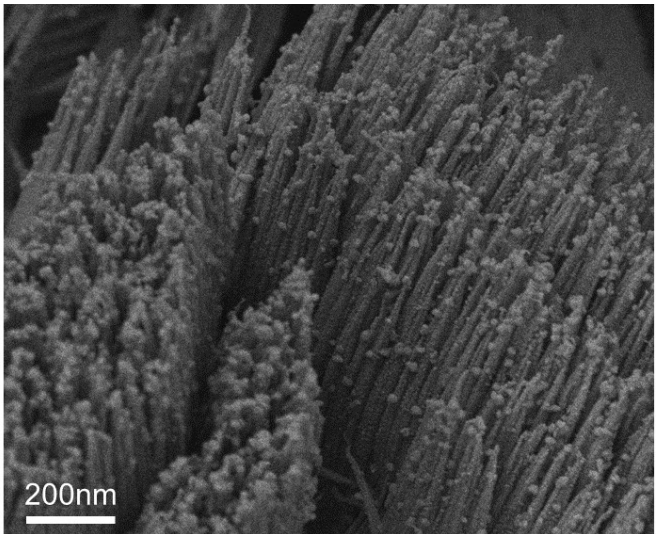

Figure S14. SEM of the Ru-$NiCo_2O_4$ catalyst after HER stability.

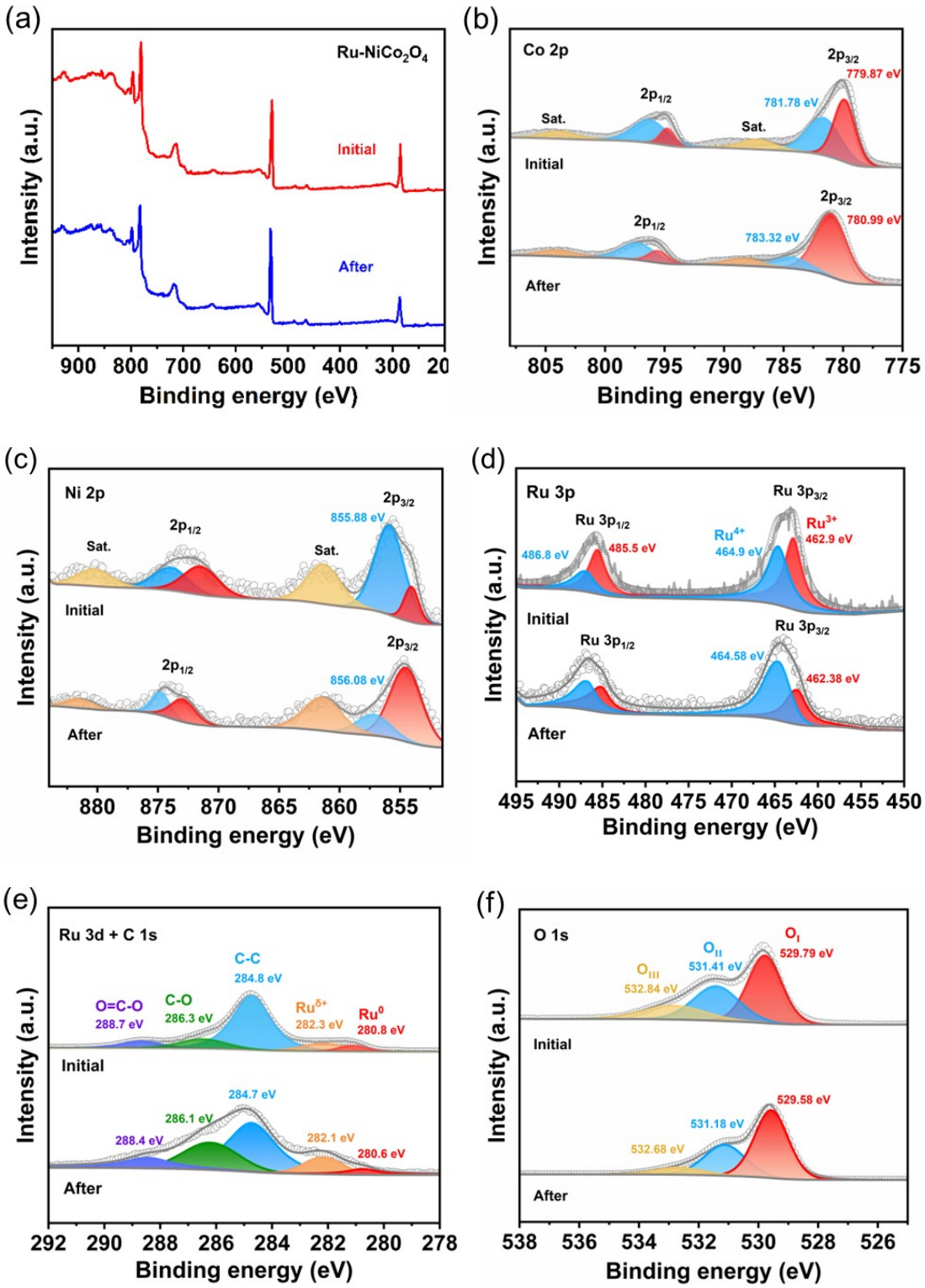

Figure S15. XPS of the Ru-$NiCo_2O_4$ catalyst after HER stability.

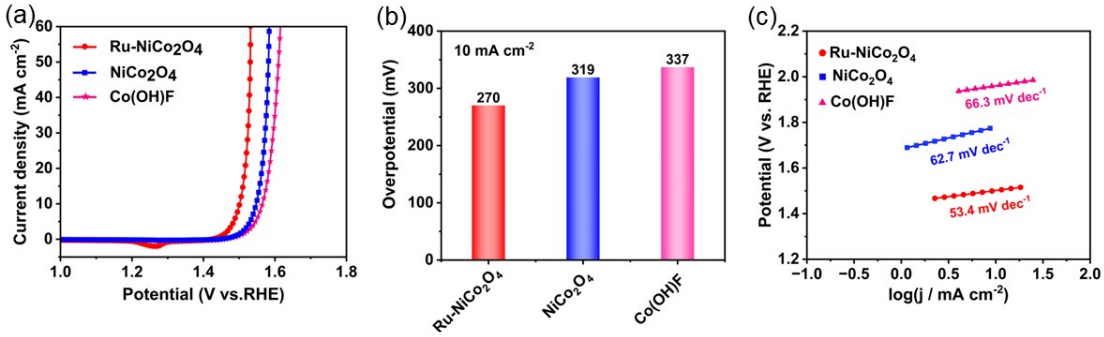

Figure S16. OER activities of the as-prepared catalysts in 1 M KOH. (a) LSV curves at a slow scan rate (0.1 mV s^{-1}), (b) the overpotentials of different electrodes required for 10 mA cm^{-2} current density, (c) Tafel plots.

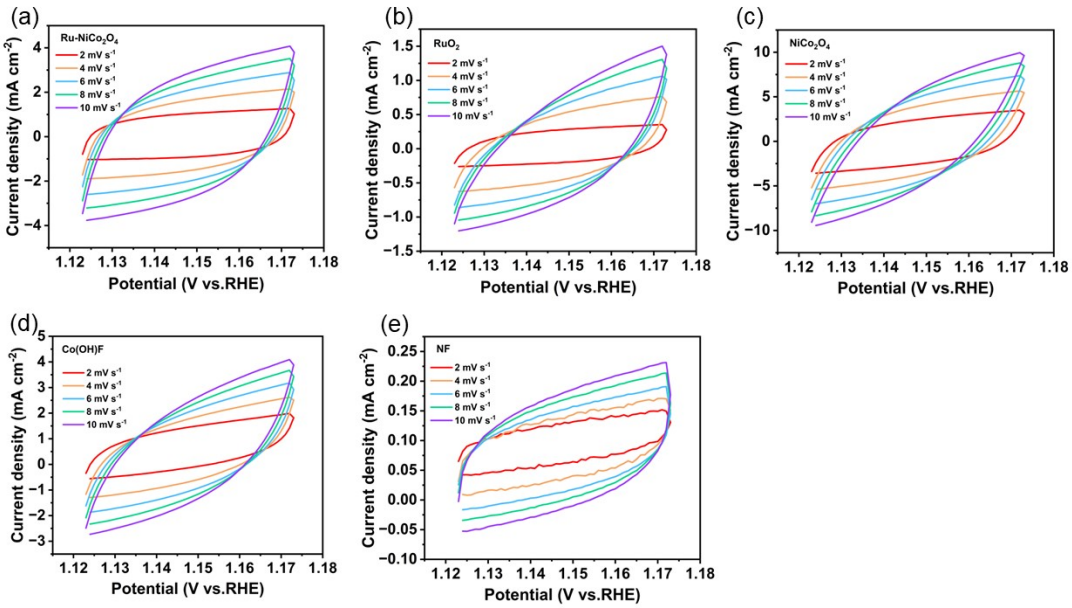

Figure S17. CV curves of the catalysts recorded in the region of 1.123V-1.173V for OER in 1 M KOH. (a) Ru-$NiCo_2O_4$, (b) RuO_2, (c) $NiCo_2O_4$, (d) Co(OH)F, (e) NF.

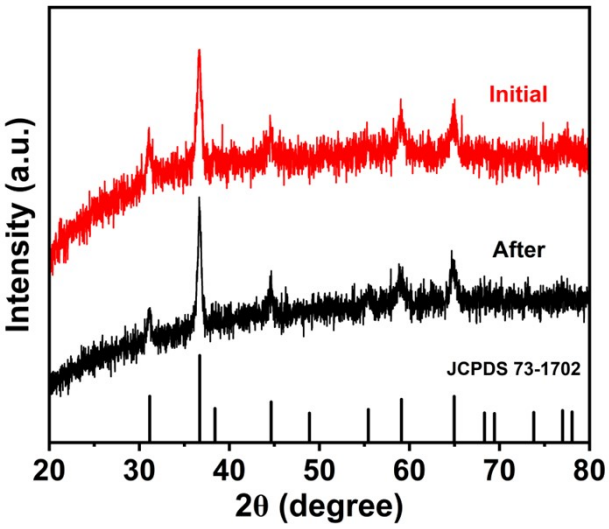

Figure S18. XRD of the Ru-$NiCo_2O_4$ catalyst after OER stability.

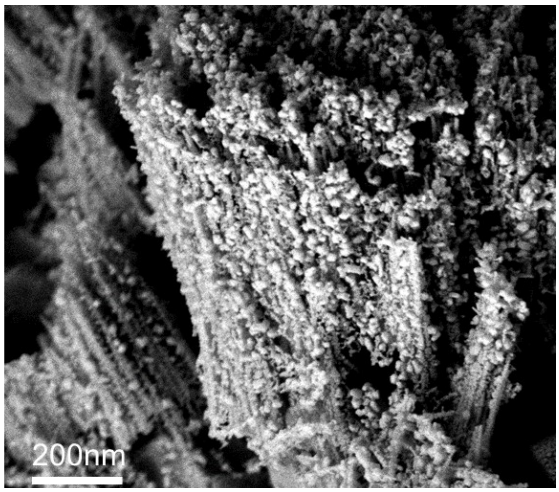

Figure S19. SEM of the Ru-$NiCo_2O_4$ catalyst after OER stability.

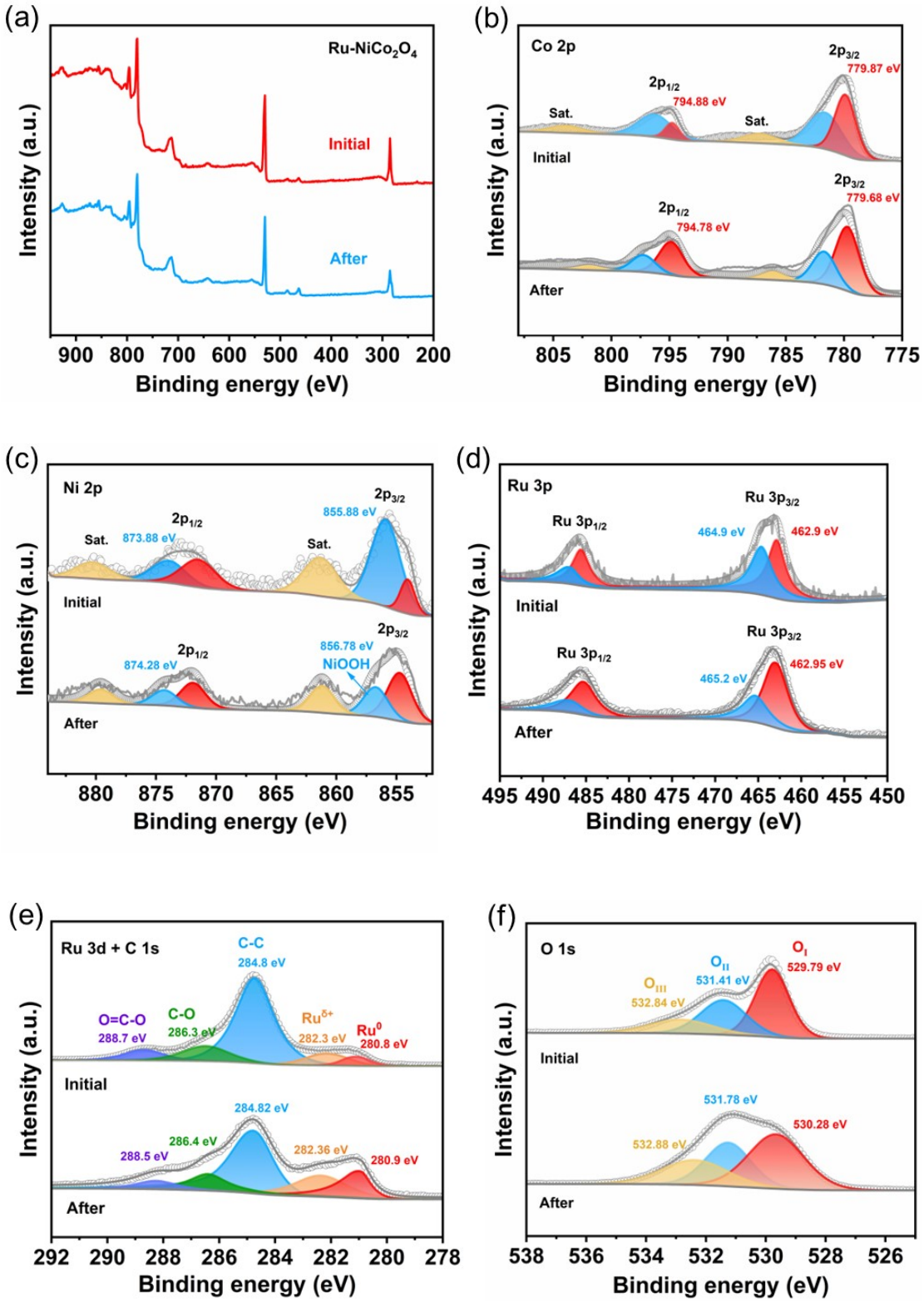

Figure S20. XPS of the Ru-$NiCo_2O_4$ catalyst after OER stability.

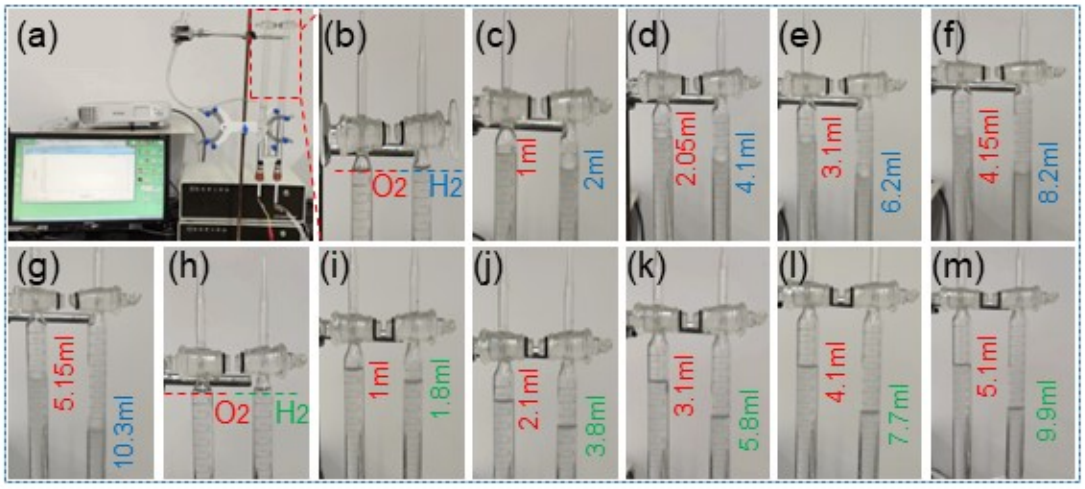

Figure S21. Overall water splitting was performed in an improved Hoffman water electrolyzer (a); Corresponding levels of H_2 (blue) and O_2 (red) gases generated at different times of 0 min (b), 5 min (c); 10 min (d); 15 min (e); 20 min (f); 25 min (g) for Ru-$NiCo_2O_4$. H_2 (green) and O_2 (red) gases generated at 0 min (h); 5 min (i); 10 min (j); 15 min (k); 20 min (l); 25 min (m) for $NiCo_2O_4$.

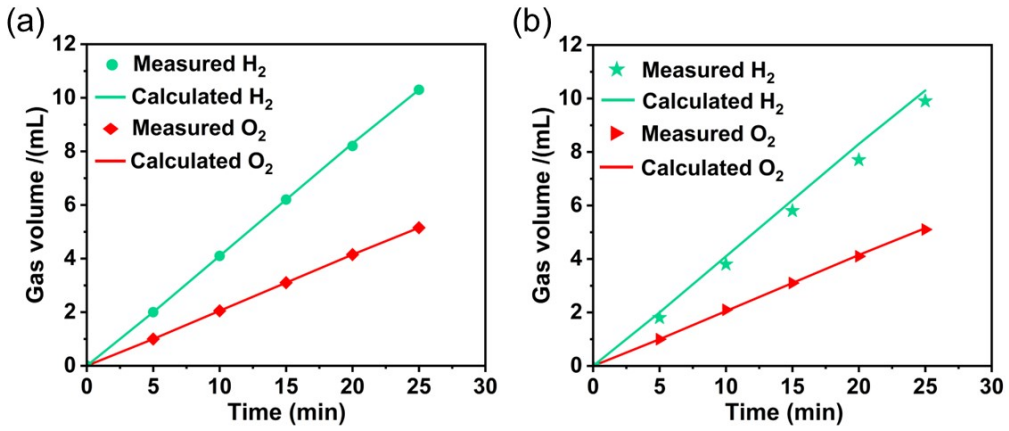

Figure S22. Experimental and theoretical volumes of the generated H_2 and O_2 by the (a) Ru-$NiCo_2O_4$, (b) $NiCo_2O_4$ electrode in a Hoffman water electrolyzer at a current density of 50 mA cm^{-2}.

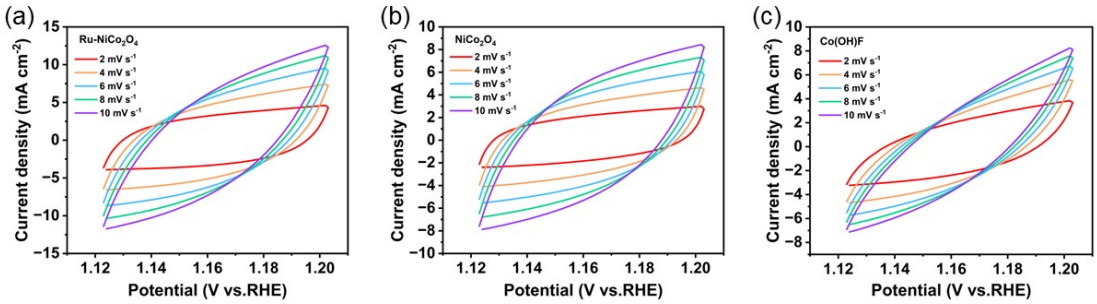

Figure S23. CV curves of the catalysts recorded in the region of 1.123V-1.203V for UOR in 1 M KOH containing 0.33 M urea.

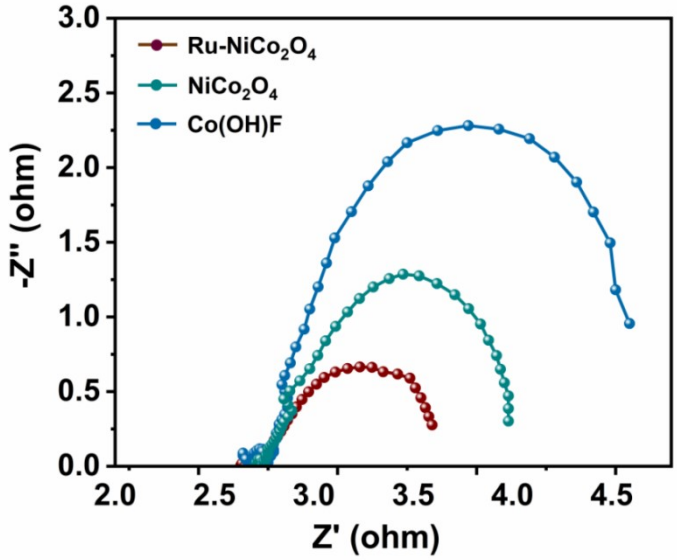

Figure S24. EIS Nyquist plots of the as prepared Ru-$NiCo_2O_4$, $NiCo_2O_4$, Co(OH)F catalysts in 1 M KOH containing 0.33 M urea.

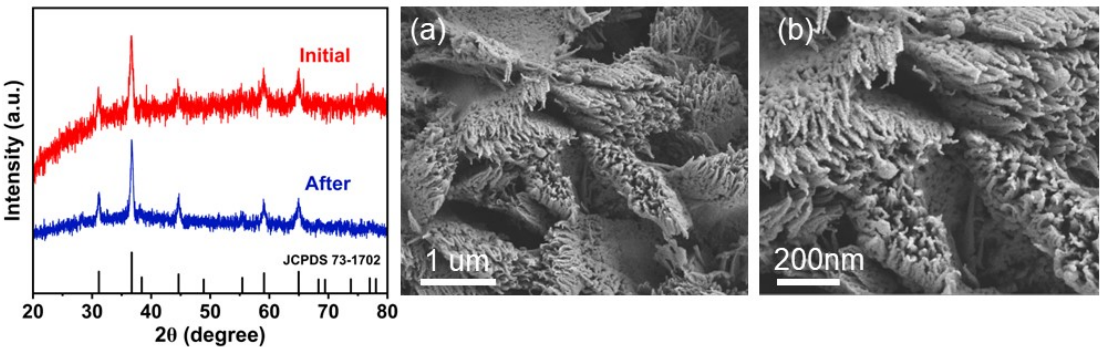

Figure S25. XRD, (a) low-resolution and (b) high-resolution SEM images of Ru-$NiCo_2O_4$ catalyst after UOR stability.

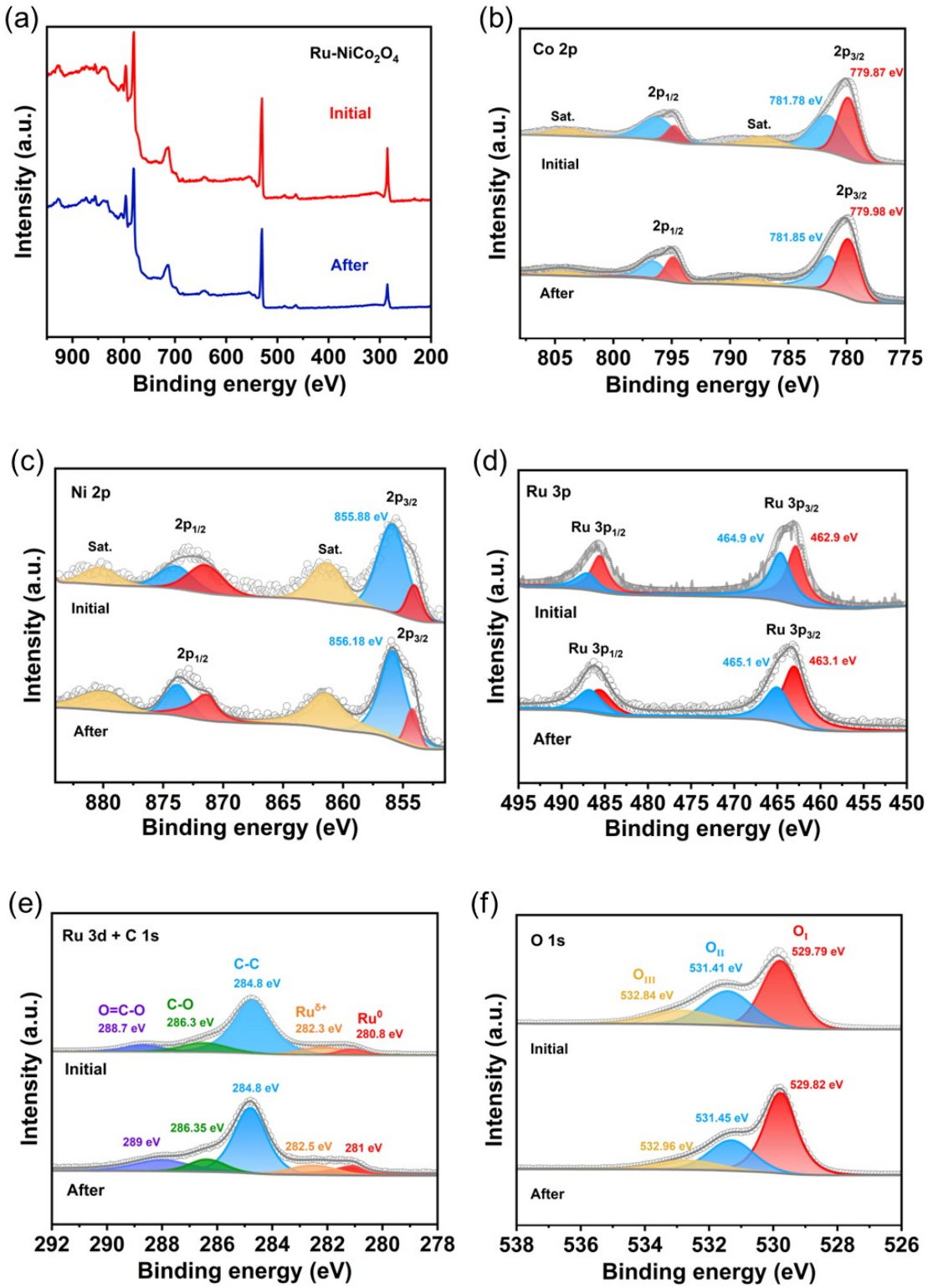

Figure S26. XPS of the Ru-$NiCo_2O_4$ catalyst after UOR stability.

Table S1. ICP-OES results of Ru-$NiCo_2O_4$ and $NiCo_2O_4$ catalysts.

Catalysts	ICP (wt. %)			
	Co	Ni	Ru	O
Ru-$NiCo_2O_4$-0.02	61.1	6.8	1.4	30.7
$NiCo_2O_4$	61.8	7.1	0	31.1

Table S2. The content of Ru in in different Ru-$NiCo_2O_4$ catalysts measured from by ICP-OES.

Samples	**content of Ru** (wt. %)
Ru-$NiCo_2O_4$-0.01	0.3%
Ru-$NiCo_2O_4$-0.015	0.8%
Ru-$NiCo_2O_4$-0.020	1.4%
Ru-$NiCo_2O_4$-0.025	3.7%
Ru-$NiCo_2O_4$-0.03	8.2%

Table S3. TOFs of Ru-$NiCo_2O_4$ and $NiCo_2O_4$ catalysts in HER and OER process.

Samples	**Ru-$NiCo_2O_4$**	**$NiCo_2O_4$**
n (mol)	2.31×10^{-6}	3.953×10^{-6}
HER (100 mV)	$j = 6.24 \times 10^{-2}$ (A cm^{-2})	$j = 2.472 \times 10^{-3}$ (A cm^{-2})
OER (300 mV)	$j = 8.268 \times 10^{-2}$ (A cm^{-2})	$j = 9.832 \times 10^{-3}$ (A cm^{-2})
HER TOF (s^{-1})	1.399×10^{-1}	3.24×10^{-3}
OER TOF (s^{-1})	9.27×10^{-2}	6.433×10^{-3}

Table S4. Comparison of HER performance for Ru-$NiCo_2O_4$ with the recently reported transitional metal-catalysts in 1 M KOH solution.

Catalysts	η= 10 mA cm^{-2} /mV	Tafel slope mV/dec	Mass loading (mg/cm^2)	References
Ru-$NiCo_2O_4$	**25**	**43.4**	**0.73**	**This work**
S-Co_2P@Ni_2P	43	58.7	2.1	Chem. Eng. J. 439 (2022) 135743
$NiCo_2O_4$/Ni_2P	45	45	1.58	Adv. Mater. Interfaces 4 (2017) 1700481.
P-Ru-CoNi-LDH	29	69	N.A.	Small., 2022, 18, 2104323
$RuNi_1Co_1$@CMT	78	77	1.6	J. Colloid Interf. Sci. 612 (2022) 710-721
Ru-NiCoP	32.2	61	N.A.	J. Colloid Interf. Sci. 612 (2022) 710-721
P-$CoNi_2S_4$	84	91	14.8	Appl. Surf. Sci. 610 (2022) 213-220
Ru-Ni_3N@NC	43	70	N.A.	Int. J. Hydrogen Energy 47 (2022) 25081-25089
Ru/Co_4N-CoF_2	53	144.1	3.5	Chem. Eng. J. 414 (2021) 128865
$MSOR_1$	43	63.1	N.A.	Adv. Funct. Mater. 33 (2023) 2210939
MH-TMO	70	97.9	2.1	Adv. Energy Mater. 12 (2022) 2200067
NiCo foam	86	62.1	N.A.	Appl. Catal. B-Environ. 288 (2021) 120002
CoMoNx-500 NSAs/NF	91	70.3	1.35	Chem. Eng. J. 411 (2021) 128433
Fe-Ni_3S_2@$FeNi_3$	105	69	0.82	Chem. Eng. J. 396 (2020) 125315
$NiCo_2O_4$@$NiMo_2S_4$	159	53.1	2.4	Adv. Mater. Interfaces 6 (2019) 1901308
NiCoFe-PS	97.8	51.8	N.A.	Small 15 (2019) 1905201

N.A. represents the unknown data.

Table S5. Comparison of the performance for Ru-$NiCo_2O_4$ with the recently reported UOR electrocatalysts in 1 M KOH solution with 0.33 M urea.

Catalysts	Potential (V) at J=10 mA cm^{-2}	Tafel slope mV/dec	Mass loading (mg/cm^2)	References
Ru-$NiCo_2O_4$	**1.316**	**47.7**	**0.73**	**This work**
Ce-Ni_2P	1.406	53.7	1	J. Alloys Compd. 912 (2022) 165234
NiFeMo	1.38	43.3	N.A.	Appl. Surf. Sci. 552 (2021) 149514
Fe-Ni_3S_2@$FeNi_3$-8	1.4	29	0.82	Chem. Eng. J. 396 (2020) 125315
NiMoSe/NF	1.39	43.3	N.A.	Int. J. Hydrogen Energy., 46 (2021) 37792-37801
P-NiFeOxHy	1.37	72.6	6.5	J. Colloid Interface Sci. 631 (2023) 56-65
V-Ni_3N/NF	1.361	N.A.	N.A.	J. Mater. Chem. A 9 (2021) 4159-4166
NiF_3/Ni_2P@CC-2	1.36	4	33	Chem. Eng. J. 427 (2022) 130865.
4-Ni/CS	1.369	39	0.35	New J. Chem. 47 (2023) 7399-7409
S-NiMo/NF	1.35	42	N.A.	Appl. Surf. Sci. 600 (2022) 154116
NiO-NiPi	1.349	70.6	0.16	Chem. Eng. J. 425 (2021) 130514
NiCo BMHs	1.33	48	N.A.	Appl. Surf. Sci. 604 (2022) 15448
$(Ni_{0.25}Fe_{0.75})_3S_2$/NF	1.38	87.8	15.6	ACS Appl. Energy Mater. 5 (2022) 1183-1192
NiFe$(OH)_2$-SD/NF	1.32	62	N.A.	J. Colloid Interface Sci. 557 (2019) 10-17

N.A. represents the unknown data.

Table S6. Comparison of cell voltage for urea electrolysis of the Ru-$NiCo_2O_4$ with previous work.

Catalysts	Cell voltage (V) at J=10 mA cm^{-2}	Mass loading (mg/cm^2)	References
Ru-$NiCo_2O_4$	**1.427**	**0.73**	**This work**
V-$FeNi_3N/N_{i3}N$	1.46	N.A.	ACS Appl. Mater. Interfaces 13 (2021) 57392-57402
Fe, V-NiS/NF	1.45	5.82	J. Ind. Eng. Chem. 113 (2022) 170-180.
Fe-Ni_3S_2@$FeNi_3$-8	1.5	0.82	Chem. Eng. J. 396 (2020) 125315
NiFeSbP/GB	1.54	N.A.	ACS Appl. Energy Mater. 5 (2022) 15689-15700
Rh-Ni	1.44	2	J. Power Sources 196 (2011) 9579-9584
$CoMn/CoMn_2O_4$	1.51	3	Adv. Funct. Mater. 30 (2020) 2000556
NiCo alloy	1.53	10	Sci. Rep. 4 (2014) 5863
MoO_2-MoO_3/Ni_2P/NF	1.44	N.A.	J. Colloid Interface Sci. 614 (2022) 337-344
NF@Acid-H_2	1.49	0.5	Appl. Surf. Sci., 496 (2019) 143710
Fe-doped NiS–NiS_2	1.55	1	Small 18 (2022) 2106841
Ni_9S_8/CuS/Cu_2O	1.47	N.A.	Int. J. Hydrogen Energy. 46 (2021) 20950-20960
Ni_3N NA/CC	1.44	1.90	Inorg. Chem. Front. 4 (2017) 1120-1124
S-NiMo/NF	1.574	N.A.	Appl. Surf. Sci. 600 (2022) 154116

N.A. represents the unknown data.